



This is a repository copy of *Benefits of using multiple Raman laser wavelengths for characterizing defects in a UO₂ matrix.*

White Rose Research Online URL for this paper:

<https://eprints.whiterose.ac.uk/184411/>

Version: Published Version

Article:

Karcher, S., Mohun, R., Olds, T. et al. (7 more authors) (2022) Benefits of using multiple Raman laser wavelengths for characterizing defects in a UO₂ matrix. *Journal of Raman Spectroscopy*, 53 (5). pp. 988-1002. ISSN 0377-0486

<https://doi.org/10.1002/jrs.6321>

Reuse

This article is distributed under the terms of the Creative Commons Attribution (CC BY) licence. This licence allows you to distribute, remix, tweak, and build upon the work, even commercially, as long as you credit the authors for the original work. More information and the full terms of the licence here:

<https://creativecommons.org/licenses/>

Takedown

If you consider content in White Rose Research Online to be in breach of UK law, please notify us by emailing eprints@whiterose.ac.uk including the URL of the record and the reason for the withdrawal request.



eprints@whiterose.ac.uk
<https://eprints.whiterose.ac.uk/>

RESEARCH ARTICLE

Benefits of using multiple Raman laser wavelengths for characterizing defects in a UO_2 matrix

Samuel Karcher¹ | Ritesh Mohun² | Travis Olds³ | Marc Weber⁴ |
Kyle Kriegsman⁵ | Xiaodong Zhao^{1,5} | Xiaofeng Guo^{1,4,5} | Claire Corkhill² |
David Field^{1,3} | John McCloy^{1,2,3,4,5} 

¹Materials Science and Engineering Program, Washington State University, Pullman, Washington, USA

²Department of Materials Science and Engineering, The University of Sheffield, Sheffield, UK

³School of Mechanical and Materials Engineering, Washington State University, Pullman, Washington, USA

⁴Institute of Materials Research, Washington State University, Pullman, Washington, USA

⁵Department of Chemistry, Washington State University, Pullman, Washington, USA

Correspondence

John McCloy, School of Mechanical and Materials Engineering, Washington State University, Pullman, WA, USA.
Email: john.mccloy@wsu.edu

Funding information

U.S. Department of Energy, Grant/Award Numbers: 89304017CEM000001, DE-NE0008689

Abstract

Raman spectroscopy is one of the most useful techniques for studying the structure of UO_2 and changes due to specific defects caused by doping, changes in stoichiometry, irradiation, or heating under oxidizing conditions. In this paper, we illustrate several aspects of the application of Raman techniques to the study of UO_2 , including the use of wavelength-dependent excitation (455, 532, and 785 nm) to assess the effects of doping (Nd, Th, and Zr), ion irradiation, and in situ heating and oxidation (UO_2 to U_3O_8). Additionally, we show examples of how correlative microscopy is possible using electron backscatter diffraction combined with Raman maps of specific vibration bands or of laser-induced luminescence generated by rare-earth dopants in the matrix. For each of these applications, we suggest optimal excitation wavelengths that vary depending on the desired data. Blue (455 nm) excitation tends to promote oxidation even at low powers, but because Raman spectra change little with doping, irradiation-induced changes are easier to observe. Green (532 nm) excitation is optimal for observing electron–phonon resonance effects in UO_2 and offers a good compromise for high-temperature oxidation experiments, delivering high-quality spectra for both UO_2 and U_3O_8 . Infrared (785 nm) excitation is best for observing “defect” bands associated with doping in UO_2 , as changes with irradiation are small. Raman spectroscopy is particularly suited for studying the stability of UO_2 towards oxidation in the presence of dopants simulating fission products, where electron–phonon resonant effects, dopant ion luminescence, and mapping can be used together to investigate structural rearrangement as a function of temperature. These techniques can offer insight into microstructural changes in UO_2 fuels at higher burnups envisioned in future reactors.

KEYWORDS

luminescence, multiwavelength Raman, Raman mapping, U_3O_8 , UO_2

This is an open access article under the terms of the Creative Commons Attribution License, which permits use, distribution and reproduction in any medium, provided the original work is properly cited.

© 2022 The Authors. *Journal of Raman Spectroscopy* published by John Wiley & Sons Ltd.

1 | INTRODUCTION

Raman spectroscopy has been used extensively to study the structure of uranium oxides and defects caused by rare-earth doping, oxidation, irradiation, isotope enrichment, and the formation of surface alteration secondary phases.^[1–6] UO_2 is particularly well-suited for study with Raman spectroscopy, because the perfect fluorite lattice has only a few Raman active modes, but anion-related defects in UO_2 generate many more. Pure UO_2 has a sharp T_{2g} Raman mode at 445 cm^{-1} and the first-order longitudinal optical (1LO) mode at 575 cm^{-1} . Additionally, strong electron–phonon coupling observed in UO_2 allows interrogation of deeper insight into its structure through resonant Raman excitation experiments,^[7–9] where certain modes are enhanced by excitation at particular energies relative to the electronic band gap. As UO_2 fuels are polycrystalline ceramics, spectroscopic mapping studies allow possible differentiation of surface oxidation states in different grains that affect degradation of spent fuel in wet storage.^[10,11] Finally, because many of the important fission products generated in neutron-irradiated UO_2 fuel are lanthanides (e.g., Nd),^[12] and trivalent lanthanides in particular have many characteristic luminescence transitions that can be excited by typical lasers used in modern Raman spectroscopy instruments,^[13] this combination allows consideration of luminescence mapping in concert with Raman mapping as a technique for identifying locations of potential concentration of certain elements.

Uranium oxides have been widely studied in the context of nuclear power generation and spent nuclear fuel disposal.^[4,14,15] Fuel dissolution rates are heavily influenced by the hyperstoichiometry of UO_2 (i.e., UO_{2+x}).^[16,17] As x increases, the excess oxygen is incorporated into interstitial sites in the cubic lattice.^[18] When x increases above 0.25, excess oxygen atoms begin to form ordered cuboctahedral-type clusters, which can be described as intermediate phases, that is, U_4O_9 ($\text{UO}_{2.25}$), that continue to maintain the cubic structure, or U_3O_7 ($\text{UO}_{2.33}$), which has a tetragonal structure.^[4,19] The transition to U_3O_8 ($\text{UO}_{2.66}$) is more significant, but there are distinct crystallographic transformation pathways from UO_2 to U_3O_8 (orthorhombic or hexagonal, depending on the temperature^[20]) as oxygen increases.^[21] The effect of dopants, which in fuels may be fission products, on the oxidation behavior of UO_2 has been shown to be significant and variable with the dopant.^[1,16,22]

As the main matrix for oxide nuclear fuel, UO_2 is irradiated in power reactors, creating fission products (such as lanthanide rare-earth metals, zirconium, etc.), which can be incorporated in the lattice and cause various oxygen stoichiometry defects that ultimately affect the long

term aqueous chemical corrosion.^[12,23] In UO_{2+x} , excess oxygen can produce U^{5+} and U^{6+} , leading to the eventual formation of highly soluble uranyl ions (UO_2^{2+}) at the surface, which can increase overall dissolution rates by orders of magnitude. With trivalent dopants (e.g., Ce^{3+} , Gd^{3+} , and La^{3+}), lattice distortion due to local charge compensation slows oxidation from UO_{2+x} to U_3O_8 by inhibiting the transition from cubic to orthorhombic. Doping with Gd^{3+} also reduces dissolution rates in both oxidizing and reducing conditions^[24,25] and changes the kinetics and temperature for the different oxidation steps.^[16]

Pure UO_2 nominally has an infrared (IR)-active T_{1u} transverse optical (TO) mode at 278 cm^{-1} , as well as the sharp T_{2g} Raman mode at 445 cm^{-1} . The 1LO mode is located at 575 cm^{-1} , and increasing intensity of the 1LO band indicates reduced symmetry of the cubic fluorite lattice structure.^[26] A second-order longitudinal optical (2LO) band can also be observed at 1150 cm^{-1} . The intensity of the 2LO band decreases with increasing defect concentration and is very sensitive to oxidation,^[27,28] as well as excitation wavelength due to the electron–phonon coupling in UO_2 .^[9] The presence of defects relaxes the selection rules and gives rise to additional Raman features, primarily in the $500\text{--}700\text{ cm}^{-1}$ range, in what is generally referred to as the “defect band.” This broad band can be deconvoluted into three regions with centers roughly at 540 , 575 , and 630 cm^{-1} . The 540 and 630 cm^{-1} bands have been assigned respectively to oxygen vacancies (V_{O}) and interstitial oxygen clusters with structures similar to U_4O_9 .^[2,4,29,30] A nearby band forms at 640 cm^{-1} from irradiation damage.^[31–33] The intensity of these bands increases as the concentration of the corresponding defect increases.

The 2LO band in particular, and other bands as well, show a pronounced excitation wavelength dependence,^[1] with an intensity increase due to resonant interaction with the electronic band gap.^[9] Band gaps varying from 1.8 (689 nm) to 2.4 eV (517 nm) have been calculated for UO_2 , with experiments favoring 2.1 eV (590 nm).^[34] This band gap is near the typical green lasers used in Raman spectroscopy (e.g., 532 or 514 nm), and hence large resonance effects are normally observed with excitation at these energies.

Additionally, Raman spectra collected over an area with an automated XY movement stage can be compiled into maps with profiles such as peak height or chemical identification of different regions using reference spectra.^[35–37] Depending on the stage movement resolution, microscope objective, and laser wavelength being used, maps with submicrometer resolution are possible. For instance, Raman mapping has been used with UO_2 to measure many grains and compare T_{2g} intensities with

crystallographic orientations measured by electron backscatter diffraction (EBSD), in order to investigate correlations between Raman signatures and grain orientations.^[38–40]

In situ experiments provide additional insight into defects bands measured by Raman spectroscopy. Elorrieta et al.^[3] used increased laser power to deliberately oxidize UO_2 and observed the development of new bands at 160 and 630 cm^{-1} . In a Raman study of U_4O_9 , Desgranges et al.^[41] concluded that the 160 cm^{-1} band indicates the presence of a U_4O_9 phase, while the 630 cm^{-1} band is characteristic of cuboctahedral oxygen clusters corresponding to hyperstoichiometric UO_{2+x} . Using a similar laser oxidation study, it was shown that substituting Th into UO_2 increases its oxidation resistance.^[42] In a study by Mohun et al.,^[32] UO_2 pellets were exposed to an aerated H_2O environment and then irradiated with He^{2+} at 45 MeV. In situ Raman measurements were performed using fiber optic cables to distance sensitive electronics from the ion beam. Three new defect peaks, resulting from the accumulation of irradiation-induced damage, were observed in the broad defect band area.

In the following, we give several extended case study examples of the application of Raman spectroscopy as a powerful tool in assessing uranium oxides. First, we show the importance of consideration of the laser wavelength and its effect on the presence and relative intensity of the various bands. Next, we show some insights gained on doping with tetravalent cations (Zr^{4+} and Th^{4+}) and their different effects on UO_2 as determined by Raman spectroscopy. We next explore the changes in the measured spectra due to ion irradiation of various doped UO_2 (Ce^{3+} , Nd^{3+} , and Yb^{3+}) and consider how these irradiation-induced defects differ from the doping-induced defects. We then show an example of an in situ oxidation measurement using a heat stage and the importance of laser wavelength choice for this experiment. Finally, we show two examples of Raman microstructural mapping, the first using ratios of characteristic Raman peaks, and the second using a laser-induced luminescence signature in Nd^{3+} -doped UO_2 .

2 | EXPERIMENTAL

2.1 | Sample synthesis

UO_2 was prepared using the nitrate precipitation method, as described previously.^[11] For doped samples, the respective nitrate salt was added to the uranyl nitrate solution. Ammonium peroxide was then added to the aqueous nitrate solution until a pH of 9 was reached. The

precipitate was filtered, dried and calcined at 800°C for 4 h in a horizontal tube furnace under gas flow, 4% H_2 by volume with the balance Ar. Calcined powder was milled in a zirconia vial for 10 min, then 8 mm diameter pellets were pressed from 0.3 g powder each at a pressure of 660 MPa. The pellets were sintered at 1700°C for 4 h in 4% H_2/Ar gas, with temperatures changed at a ramp and cooling rate of 5°C/min. A gas bubbler was used to verify the pellets remained in a reducing atmosphere during sintering. A U_3O_8 pellet was also produced by the same method, by sintering in air instead of a hydrogen environment.

UO_2 pellets doped with Th and Zr were prepared by the same co-precipitation and sintering methods. Zr-doped UO_2 was prepared with 1.6 at.% and 6.7 at.% Zr (nominally 1 at.% and 5 at.%) as measured by electron probe microanalysis (EPMA) (JEOL JXA-823). Th doped samples were made with 1 at.% and 5 at.% nominally. Subsamples were subsequently hydrothermally oxidized by placing them in a Parr reaction vessel with deionized water for 18 h at 100°C. Additionally, samples of $\text{U}_{1-y}\text{Nd}_y\text{O}_{2-x}$ ($y = 0.05\text{--}0.40$, nominally) were synthesized using the same methods described above.

In preparation for Raman mapping and scanning electron microscopy (SEM) analysis, one sintered pellet was mechanically polished using 1 μm diamond suspension. This pellet was subjected a second identical sintering run after polishing to further anneal the pellet ensuring near-stoichiometric UO_2 and minimizing residual strains at the surface.

Samples of previously described^[11] lanthanide-doped UO_2 were irradiated at the Dalton Cumbrian Facility, United Kingdom. Eight millimeter diameter pellets, ~ 2 mm thick, of undoped and (Ce, Nd, or Yb)-doped UO_2 were mounted such that one side of each pellet was exposed. Samples were exposed to 1 MeV Kr ions at room temperature with a constant fluence of 5×10^{15} ions/ cm^2 . The projected range of damage is ~ 0.25 μm at this energy (see Figure S1), leaving the backside of the pellets “pristine” for comparison.

2.2 | Microscopy

SEM analysis was performed on polished and annealed UO_2 using a field emission scanning electron microscope (FESEM, FEI/Thermo Scientific) with EBSD, energy dispersive spectroscopy (EDS), and backscatter electron (BSE) detectors. EBSD patterns were collected at 20 keV using an EDAX detector with a step size of 0.5 μm . Orientation Imaging Microscopy (OIM) Analysis 7 software was used to generate inverse pole figure (IPF) orientation maps and to calculate grain size and texture.

2.3 | Raman spectroscopy

Raman measurements were performed using a Thermo Scientific DXR2i Raman Microscope. Multiple excitation lasers were used (455, 532, and 785 nm) in depolarized and vertical-vertical polarized configurations. The 532 and 785 nm lasers each have two gratings. For all luminescence measurements, the extended range 532 nm (50–6000 and 10 cm^{-1} resolution) and standard range 785 nm (50–3500 and 4 cm^{-1} resolution) gratings were used. All other spectra were obtained using the highest resolution grating available, that is, standard grating for 532 nm (50–3500 and 4 cm^{-1} resolution), 455 nm (50–3500 and 4 cm^{-1} resolution), and high-resolution grating for 785 nm (50–1800 and 2 cm^{-1} resolution). The maximum resolution and true wavelength ranges are summarized in Table S1.

Irradiated UO_2 samples were investigated using 455 nm excitation, operated at 1 mW with a 1 s exposure; 532 nm, operated at 2 mW with a 0.5 s exposure; and 785 nm, operated at 6 mW with a 2 s exposure. These acquisition parameters were chosen to avoid surface oxidation as much as possible. A 100 \times objective was used with a 50 μm slit aperture for all three lasers. Data reduction was performed using Spectragryph^[43] to apply smoothing (Savitsky–Golay filter) and an adaptive baseline correction. Fityk^[44] was used for peak fitting and deconvolution using Voigt peak profiles.

A Linkam TS1500 heating stage was used for in situ experiments using the Thermo Scientific Raman system. UO_2 and Zr-doped UO_2 samples crushed into coarse powder were placed in platinum crucibles and heated at 5 $^\circ\text{C}/\text{min}$ up to 600 $^\circ\text{C}$. Clean air was flowed over the samples at 20 cm^3/min for the duration of the experiment. Spectra were collected using the 532 nm laser, which was found to be optimum for this experiment, in depolarized configuration with a power of 1 mW and an exposure time of 1 s. A region measuring approximately 50 $\mu\text{m} \times 50 \mu\text{m}$ was scanned containing 100 individual spectra collected within a 10 $^\circ\text{C}$ range, as heating was not paused during collection. Spectragryph was used to smooth, remove baseline, and normalize spectra.

For mapping experiments, the laser and detector were set in vertical polarized configuration. The 532 nm laser was operated at 1 mW with a 0.25 s exposure, while the 785 nm laser was operated at 20 mW with a 1 s exposure time. The 100 \times objective with 50 μm pinhole aperture was used, giving a laser spot size of 0.8 μm for the 532 nm laser and 1.2 μm for the 785 nm laser. The 455 nm laser was not used for mapping.

For luminescence experiments, the 785 nm laser was used. The power required was strongly dependent on the sample and strength of luminescence. Nd_2O_3 (99.99%,

Alfa Aesar or ProChem Inc.) was measured with 1 mW laser power and 0.01 s exposure and Nd-nitrate (Alfa Aesar) was measured with 2 mW and 0.025 s exposure. Spectra and maps from the 10 at.% Nd-doped UO_2 pellet were collected at 15 mW with 0.5 s exposure times. The maps were collected with a 1 μm step size.

2.4 | Thermogravimetric analysis

Powdered samples (~ 2 mg) were loaded into 1 ml alumina crucibles and inserted into the thermogravimetric analysis–differential scanning calorimetry instrument (TGA-DSC, Setaram SetSYS-2400) for analysis. Thermal decomposition experiments of undoped and selected doped UO_2 were carried out in the 25–900 $^\circ\text{C}$ temperature range with a heating rate of 5 $^\circ\text{C}/\text{min}$ under synthetic air flow (20 ml/min). The sensitivity of the TGA-DSC system was calibrated using the thermal decomposition of CaC_2O_4 and melting cycles of various metals, a full description of which may be found elsewhere.^[1,45]

3 | RESULTS AND DISCUSSION

3.1 | Effect of excitation wavelength on undoped UO_2

Certain Raman-active bands in UO_2 exhibit significant variability in position and intensity depending on excitation wavelength, and analyses made with multiple excitation energies can give complementary information.^[9,27,46] Wavelength dependence is clearly seen when comparing undoped UO_2 measured with multiple wavelengths (Figure 1a). Here, Raman spectra were trimmed between 200 and 1500 cm^{-1} before applying a smoothing and background subtraction, then spectra were normalized to the T_{2g} band intensity to allow easier qualitative comparison. Unprocessed spectra for the entire collected wavenumber range are shown in Figure S6. The 2LO band intensity at 1150 cm^{-1} is roughly one order of magnitude higher when using the 532 nm laser than with the 455 nm laser and is barely distinguishable from background when using the 785 nm laser. Relative to other bands, the T_{2g} band has very high intensity when using the 785 nm laser.

The calculated electronic band gap of UO_2 is 2.3 eV,^[47] and the experimental band gap is 2.1 eV,^[8,48] which are both close to the 2.33 eV resulting from the 532 nm laser excitation. Livneh and Sterer^[9] show that the LO bands are activated via resonance and that the signal from incident energies close to the band gap are more intense than energies further away. Longer

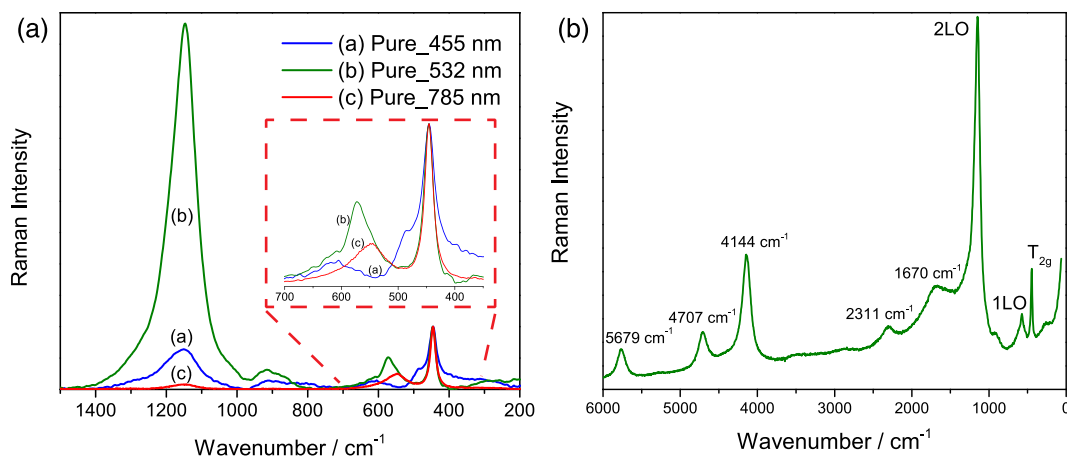


FIGURE 1 (a) Undoped UO_2 Raman spectra using three different excitation wavelengths, smoothed, trimmed, background corrected, and normalized to the T_{2g} peak intensity. (b) Undoped UO_2 measured with extended range grating on 532 nm laser. Uncorrected data shown [Colour figure can be viewed at wileyonlinelibrary.com]

excitation wavelengths (e.g., 633 and 785 nm) have energies below the UO_2 band gap (1.96 and 1.58 eV, respectively), so more light is scattered and the Raman signals are more intense. Excitation wavelengths with similar energy to the band gap result in a lower Raman signal, but an increase in the intensity of the resonance activated LO bands. Livneh and Sterer^[9] also observed that the even-numbered LO bands are both more intense and more polarized than the odd-numbered LO bands.

The intensity of defect related bands in the 500–700 cm^{-1} region (Figure 1a inset) also depends strongly on the excitation wavelength. Defect bands are fairly weak when measured with the 455 nm laser, with only the band at 630 cm^{-1} being observed. The intensity of this band is likewise weak when using the 532 nm laser, but the signal from the 1LO peak at 575 cm^{-1} is more prominent. The 785 nm laser does not appear to activate the 630 cm^{-1} band in the defect region in oxidized samples, but instead leads to moderate activation of

the 540 cm^{-1} band, and in irradiated samples, the 640 cm^{-1} band.

The 630 cm^{-1} band, as previously mentioned, corresponds to interstitial oxygen clusters in hyperstoichiometric UO_2 . The surface of UO_2 can quite easily oxidize due to heating from the excitation laser. This phenomenon was intentionally used by Elorrieta et al.^[3] to study the in situ laser-induced oxidation of UO_2 . In the current set of experiments, power was set low with each laser to avoid damaging the surface, although the samples were noticeably more susceptible to oxidation using the 455 nm laser than the 532 or 785 nm lasers, so minor laser-induced damage may have occurred. U_3O_8 spectra include peaks around 800 cm^{-1} and a triplet at around 350, 415, and 480 cm^{-1} . In Figures 1b and 2a, broadening and asymmetry of the T_{2g} band are observed as a result of these overlapping U_3O_8 bands. Another defect band around 800–1000 cm^{-1} is present and can be attributed to U_3O_8 or uranyl $[(\text{U}^{6+}\text{O}_2)^{2+}]$, which has a Raman band

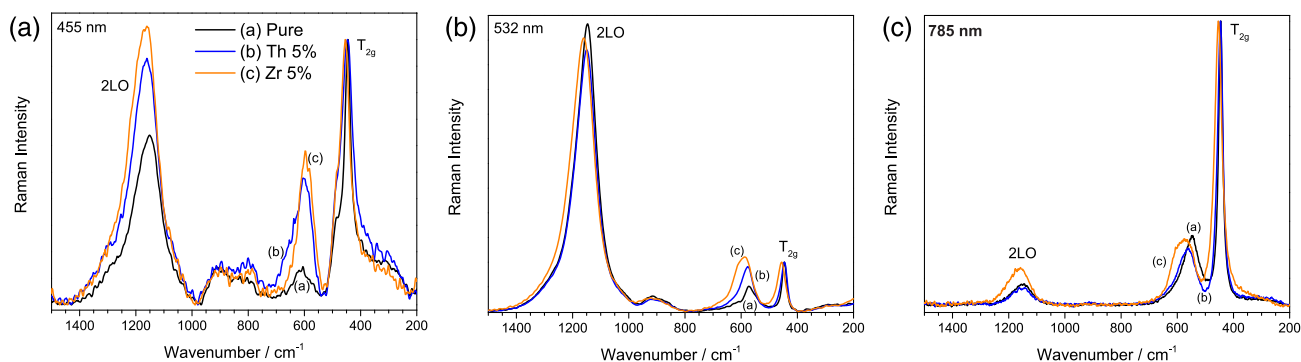


FIGURE 2 Raman spectra of 5% target Th- and Zr-doped and undoped UO_2 with different laser excitations: (a) 455, (b) 532, and (c) 785 nm [Colour figure can be viewed at wileyonlinelibrary.com]

around 870 cm^{-1} ,^[49,50] although a similar feature $\sim 877\text{ cm}^{-1}$ has also been assigned to U_4O_9 .^[8] These bands suggesting oxidation are strongest with 455 nm excitation and present in some 532 nm spectra.

To our knowledge, Raman bands above 1600 cm^{-1} are rarely discussed in the UO_2 ceramic fuel literature. Livneh and Sterer^[7,9] showed that higher order LO bands exist and are present at ~ 1725 , 2312, 2910, and 3470 cm^{-1} . In the current study, an extended range grating was also used in combination with the 532 nm laser to allow spectral data collection from 50 to 6000 cm^{-1} . The raw uncorrected spectrum is shown in Figure 1b. Using this laser and grating combination, five other peaks are observed; two broad weak bands at 1670 and 2311 cm^{-1} , a stronger peak at 4144 cm^{-1} , and two less prominent peaks at 4707 and 5769 cm^{-1} . These bands have been previously identified and attributed to ${}^3\text{F}_2(\Gamma_5)$, ${}^3\text{F}_2(\Gamma_3)$, and ${}^3\text{H}_5(\Gamma_4)$ bands resulting from resonant electronic interactions with LO phonons in UO_2 .^[7,51]

3.2 | Effect of Th and Zr doping

In Figure 2, Raman spectra of the highest doped Zr: UO_2 and Th: UO_2 , collected with all three lasers, are compared with undoped UO_2 . The T_{2g} band height was normalized to unity in all cases to compare relative intensities of the other peaks. The 455 nm laser resulted in noisier spectra even with longer collection times. The sample surface was most easily damaged by heating from the 455 nm laser and also somewhat by the 532 nm laser. In undoped samples, the T_{2g} band, defect bands, and 2LO bands have similar intensities with 455 nm excitation. With 532 nm excitation, the 2LO band is roughly $6\times$ greater than the defect band or T_{2g} band. With 785 nm excitation, the intensity of the T_{2g} peak is $5\text{--}6\times$ more intense than the defect band or the 2LO band. Hydrothermally oxidized spectra of these doped samples are shown for the 785 nm laser in Figure S1.

With 455 nm excitation, the intensity of defect bands from both doped samples is around $5\times$ higher than the undoped sample. With 532 and 785 nm, the defect band intensities of the doped samples are roughly twice that of the undoped sample. The 455 nm defect bands are comprised primarily of a 1LO component (575 cm^{-1}) and a peak around 600 cm^{-1} associated with MO_8 -type clusters where M is a metal cation other than U.^[52] The 532 nm spectra show increased 1LO intensity with doped samples, but the other defect bands are weaker in comparison.

The defect band is broader in the Zr-doped sample than the Th sample due to a larger contribution from the band $\sim 600\text{ cm}^{-1}$, most noticeable in the 532 and 785 nm excitations. As previously stated, interstitial oxygen atoms

form clusters which manifest as a defect band around $630\text{--}640\text{ cm}^{-1}$.^[30] In the Zr-doped sample, however, the main contribution is instead attributed to 8-coordinated Zr atoms forming ZrO_8 clusters,^[52,53] as also observed in fluorite-structured Zr: CeO_2 . The MO_8 (i.e., ZrO_8) type cluster signature is presumably related to ionic size mismatch, as it is not significant in the Th-doped sample because here M is a similar size to U ($r_{\text{U}^{4+}} [\text{C.N.:}8] = 1.00\text{ \AA}$ and $r_{\text{Th}^{4+}} [\text{C.N.:}8] = 1.05\text{ \AA}$, where C.N. is coordination number)^[54] and directly substitutes in the fluorite lattice as ThO_8 without significant distortion. Rao et al.^[26] used a 532 nm laser to study the Raman spectra of the $\text{ThO}_2\text{--UO}_2$ system over its entire composition range, finding that the lattice parameter varies linearly with composition, indicating direct substitution. A narrow defect band observed around 600 cm^{-1} in the non-oxidized Th-doped UO_2 likely arise from the small lattice distortion due to the slight mismatch in the 8-coordinated ionic size of Th^{4+} and U^{4+} . After oxidation (Figure S2), the defect band broadens as the oxygen interstitial band at 640 cm^{-1} grows.

The T_{2g} position shifts towards higher wavenumber as a result of lattice distortion and broadens slightly indicating an increasing concentration of local disorder, the effect being greater with Zr doping due to the larger ionic mismatch ($r_{\text{Zr}^{4+}} [\text{C.N.:}8] = 0.84\text{ \AA}$).^[54] The slope of the change in T_{2g} position with increasing dopant concentration is $0.137z$ for Th and $1.23z$ for Zr (z is dopant concentration in at.%) (see Figure S3). Note that this band becomes asymmetric with increasing Th content, due to a higher wavenumber for the T_{2g} mode in ThO_2 than in UO_2 , as also observed by others.^[26]

Deconvolution of the defect band into individual components allows quantitative comparison of the relative intensities or areas of specific defect bands. Example fits of the Th-doped samples measured with 532 nm excitation are given in Figure S4. Defect band areas are normalized by dividing by the T_{2g} area. The MO_8/T_{2g} , O_i/T_{2g} , and $2\text{LO}/T_{2g}$ area ratios calculated from 532 nm spectra are plotted in Figure S5. The undoped non-oxidized sample has a small area ratio for MO_8 and O_i (Figure S5a,b), and both ratios increase by about $3\times$ after oxidation. Considering the origin of the MO_8 band, its presence in the undoped sample and increase after oxidation result from the O_i band overlapping. In the doped samples, the MO_8/T_{2g} area ratios increase by $2\text{--}3\times$ as the dopant concentration increases, but drop after oxidation. The difference between dopant concentrations is less pronounced in oxidized samples, but the MO_8/T_{2g} ratio remains $5\text{--}10\times$ greater in Zr-doped samples than Th-doped samples.

The O_i band was not observed in doped non-oxidized samples. A small band was observed in the undoped non-

oxidized sample, which could be due to incomplete conversion to UO_2 due to short sintering time. The O_i/T_{2g} ratio increases by $3\times$ in the undoped oxidized sample. The lower concentration Th-doped sample has a ratio roughly 50% greater than the other oxidized samples. Th doping was reported to inhibit oxidation caused by Raman laser heating.^[42] This may be reflected by a smaller O_i/T_{2g} ratio in the oxidized higher Th-doped sample.

The 2LO band has been shown to be sensitive to slight oxidation and its presence at high intensity indicates a more pristine lattice structure, due to its sensitivity to the presence of defect structures.^[4,27,28] In Figure S5c, $2LO/T_{2g}$ area ratios are plotted for Th- and Zr-doped samples. The $2LO/T_{2g}$ ratio decreases by about half in the doped non-oxidized samples compared to the undoped sample. The ratio in Zr-doped samples is slightly less than Th-doped samples, possibly indicating less distortion for Th than Zr at the same concentration. The ratio is similar or slightly larger in the higher doped samples, which could indicate clustering of dopants and slightly less distortion of the fluorite lattice. In the undoped oxidized sample, the $2LO/T_{2g}$ ratio decreases by more than $4\times$ after oxidation. For doped samples, after oxidation the $2LO/T_{2g}$ ratio decreases somewhat less than the undoped, about $2\times$ in the Th-doped samples and about $1.5\times$ in the Zr-doped doped samples.

3.3 | Effect of ion irradiation on Ce-, Nd-, or Yb-doped UO_2

UO_2 pellets doped with trivalent lanthanides (Ce, Nd, or Yb) were subjected to Kr-ion irradiation, and the Raman spectra from the irradiated and “pristine” sides of the ion irradiated samples were measured using 455, 532, and

785 nm lasers. With trivalent doping, an oxygen vacancy (V_O) band forms around 540 cm^{-1} as a result of necessary charge balancing between U^{4+} and M^{3+} dopant cations.^[1,4,55] In Figure 3a, we see this band is strongest in the Ce-doped sample, with the 785 nm excitation wavelength, and is not present in the undoped sample. The Nd- and Yb-doped samples have slightly broader spectra due to overlapping 1LO band ($\sim 575\text{ cm}^{-1}$). Using other Raman excitation wavelengths (455 and 532 nm), the differences between dopants or between pristine and irradiated samples are less pronounced. Similar comparisons with the 785 nm laser are shown for Nd- and Yb-doped samples in Figure S8. The full set of Raman spectra from the irradiated samples obtained with 455, 532, and 785 nm lasers are shown in Figure S9. In Figure 3b, Raman spectra of irradiated undoped and Ce-doped UO_2 are shown.

According to calculated ion implantation profiles (Stopping and Range of Ions in Matter, SRIM^[56]), the implantation conditions result in a sufficiently high defect concentration (displacements per atom, dpa ≈ 21.3) along a depth of $\approx 0.25\text{ }\mu\text{m}$ beneath the irradiated surfaces, allowing Raman to characterize the damaged zones. When measured with the 455 nm laser (Figure S6), the overall defect band area of the irradiated side of each sample was roughly double the area of the pristine side, in good agreement with the buildup of irradiation-induced disorder in the UO_2 matrix. The change in defect band area caused by doping is least prominent with the 455 nm laser, making it easier to see the effect of irradiation directly.

Conversely, using the 785 nm laser (Figure 3b), there is a relatively small change between pristine and irradiated samples, but the difference between undoped and doped samples is more significant. Defect band areas

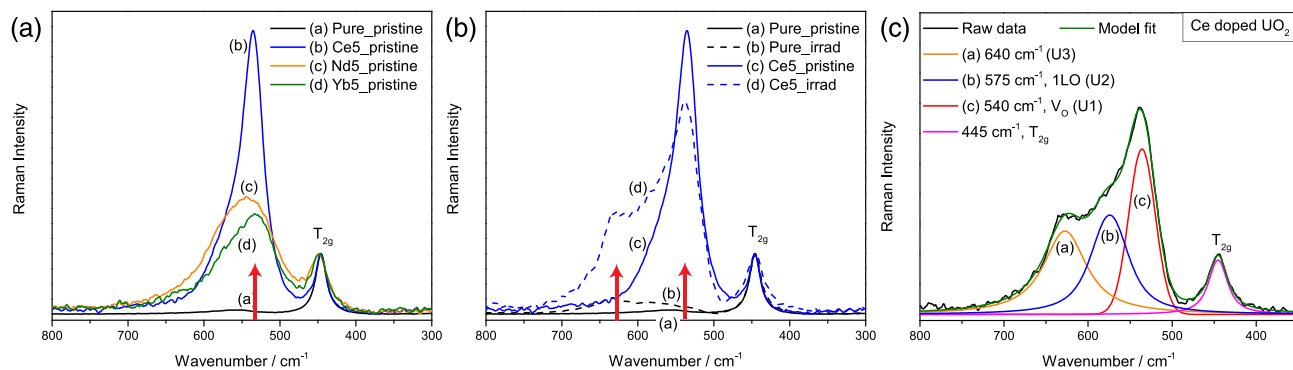


FIGURE 3 Effect of doping and ion irradiation on UO_2 ; spectra were recorded with 785 nm excitation, trimmed and background corrected, then normalized to the T_{2g} peak. (a) Comparison of undoped and trivalent ion doped UO_2 ; arrow highlights the 540 cm^{-1} band. (b) Comparison of defect bands from doping (Ce), irradiation without doping, and a combination of irradiation and doping with Ce; arrows highlight the 540 and 640 cm^{-1} bands. (c) Deconvoluted spectrum of the irradiated Ce-doped UO_2 [Colour figure can be viewed at wileyonlinelibrary.com]

from the 532 nm laser appear highly dependent on both doping species and irradiation (Figure S6). For instance, we observed that the area increases by nearly 4× for the irradiated undoped sample as a result of increasing 1LO (Figure 4a), but the initially larger 1LO band of doped samples does not increase as much with irradiation (Figure 3b). This finding suggests that the incorporation of trivalent dopants can potentially alter the irradiation-induced defect formation in UO_2 .

Upon spectral deconvolution into the 540, 575, and 630 cm^{-1} bands (referred to as U1, U2 and U3), we see that the defect bands in 455 nm pristine (pellet backside) spectra for the undoped, and all three doped samples are almost entirely U2 (i.e., 1LO), with some presence of U3 (i.e., oxygen interstitials or related defect) in irradiated spectra. The 785 nm excitation wavelength provides the strongest signal of the U1 (i.e., oxygen vacancies) band, with good resolution of the U2 and U3 bands as well (Figure 3c). The complete dataset of deconvolutions is provided in (Table S2 and Figures S7–S9).

Compared with the pristine (i.e., undoped) samples, trivalent dopants shift the T_{2g} band position towards higher wavenumber, which could be attributed to a combined effect of the unit cell contraction ($r_{\text{U}^{4+}} [\text{C.N.:8}] = 1.00 \text{ \AA}$, $r_{\text{Ce}^{4+}} [\text{C.N.:8}] = 0.97 \text{ \AA}$, and $r_{\text{Yb}^{3+}} [\text{C.N.:8}] = 0.985 \text{ \AA}$) and the formation of both oxygen vacancies and U^{5+} species ($r_{\text{U}^{5+}} [\text{C.N.:7}] = 0.84 \text{ \AA}$) to compensate for the charge. The T_{2g} band shifts towards lower wavenumbers post-irradiation compared with the pristine side, indicating an expansion of the lattice after irradiation due to defect accumulation (Table S2). This trend was also observed in He^{2+} -irradiated UO_2 measured with a 633 nm laser.^[57] The shift in T_{2g} peak position of the Ce sample is smaller compared with the other doped

samples, and negative in the 455 nm spectrum. The negative shift observed only with 455 nm excitation may be attributed in part to localized heating and oxidation caused by the laser, as oxidation causes a negative shift in T_{2g} position.^[58] This result could also be explained by the partial reduction of nominally Ce^{4+} cations to Ce^{3+} ($r_{\text{Ce}^{3+}} [\text{C.N.:8}] = 1.143 \text{ \AA}$) resulting in a lattice expansion. Similar observations have previously been reported by Palomares et al.^[59] and Cureton et al.^[60] The T_{2g} full-width half maximum (FWHM) also increases as a result of irradiation (Figure S9) and with the addition of dopants; however, the change in FWHM due to doping is less prominent with the 455 nm spectra.

Overall, it can be concluded that the effects of doping and irradiation are observable to *different extents* depending on the Raman excitation laser. Therefore, one should be cautious in assigning a quantitative assessment of defect production in UO_2 from only Raman results, particularly if comparing across studies with different Raman excitation conditions. Clearly some bands (e.g., LO bands) have Raman cross sections that have some resonant, excitation wavelength-dependent components. This is particularly true when comparing the overall defect band envelope, which contains the 1LO resonant band, or when deconvoluting this overall envelope.

3.4 | Effect of oxidation

3.4.1 | U_3O_8 : Effect of excitation wavelength on Raman spectrum

As previously described, oxidation of UO_2 progresses until the ratio of O:U reaches 2.66, resulting in

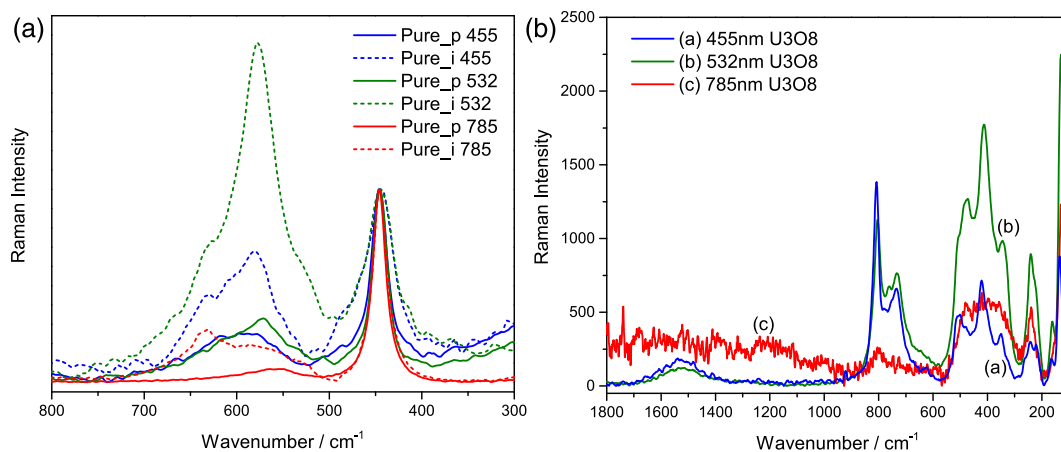


FIGURE 4 UO_2 and U_3O_8 spectra collected with 455, 532, and 785 nm excitation wavelengths. (a) Raman spectra of pristine and irradiated undoped UO_2 (p = pristine side and i = irradiated side). (b) Raman spectra of U_3O_8 [Colour figure can be viewed at wileyonlinelibrary.com]

orthorhombic U_3O_8 .^[61–63] A polished pellet of U_3O_8 was measured using 455, 532, and 785 nm Raman excitation wavelengths. Senenayake et al.^[64] measured the spectrum of U_3O_8 using 488 and 785 nm lasers, noting that with the 785 nm laser, spectra were very weak. The unprocessed spectra obtained in the current study are shown in Figure 4b. There are several intense sharp peaks below 200 cm^{-1} , observable to greater or lesser extent with all lasers, and these have recently been investigated in detail by Miskowiec et al.^[65] using a very low-power configuration allowing a low wavenumber limit of 45 cm^{-1} . The authors were able to record high-quality spectra by using a very low power ($1.5\text{ }\mu\text{W}$) over a 1 h collection time, assigning peaks to features between 54 and 800 cm^{-1} that correspond to the peaks observed in our spectra. A broad band was also observed in our samples with 455 and 532 nm lasers at $1520\text{--}1530\text{ cm}^{-1}$. Similar bands have been observed in literature at 1575 ^[66] and at 1595 cm^{-1} ^[64] but have not yet been assigned to our knowledge. Detailed peak numbers are listed in Table S4 for 455 and 532 nm lasers, and deconvolutions are shown in Figures S10 and S11.

3.4.2 | In situ heat stage Raman

In situ heating experiments were performed on the pure UO_2 and the 6.7 at.% Zr-doped UO_2 using the 532 nm laser, because it produced good spectra for both UO_2 and U_3O_8 (Figure 4). A sample of $<200\text{ mg}$ was heated to 600°C at $5^\circ\text{C}/\text{min}$ under constant air flow and Raman spectra were automatically collected every 3 min. Heating was paused at 450°C to allow recording of more spectra

during oxidation to U_3O_8 . Results, after smoothing and background correction was applied, are plotted in Figure 5a (undoped UO_2) and Figure 5b (Zr-doped UO_2).

The quality of Raman spectra obtained during in situ heating was affected by a high background while measuring at elevated temperature and reduced signal from measuring through the transparent sapphire window on the top of the heat stage. High background has been observed by others above 540°C when heating in H_2/Ar gas.^[58] This is expected due to the black-body emission of the sample at elevated temperatures.

A clear transition from UO_2 to U_3O_8 can be seen starting above 400°C by a rapid disappearance of the 2LO and 1LO bands and formation of the bands between $300\text{--}500$ and $700\text{--}800\text{ cm}^{-1}$ observed in U_3O_8 .^[2,3] These results are in good agreement with TGA on undoped UO_2 , performed in previous work, which showed an oxidation reaction occurring from 350°C to 450°C .^[1] TGA was also performed on both Zr- and Th-doped samples (Figure 5c). However, the impacts on the thermal oxidation from the two dopants are quite different. First, with Zr and Th doping, the onset of oxidation reaction moves to lower temperatures; however, both dopants slow down the rate of thermal oxidation. Particularly, the 5% Th-doped UO_2 has a much slower rate of oxidation, and although it started at $\sim 200^\circ\text{C}$, it completed its transition to U_3O_8 phase at $\sim 550^\circ\text{C}$, which is higher than that of undoped UO_2 (the transition to U_3O_8 completed by 500°C). For the Zr-doped UO_2 , because the onsets are at lower temperatures, then the oxidation reactions finish at $\sim 450^\circ\text{C}$ and $\sim 400^\circ\text{C}$, for the 1.6 at.% and the 6.7 at.% Zr-doped UO_2 , respectively. The lower onset temperature can be due to the potential formation of U_4O_{9+y}

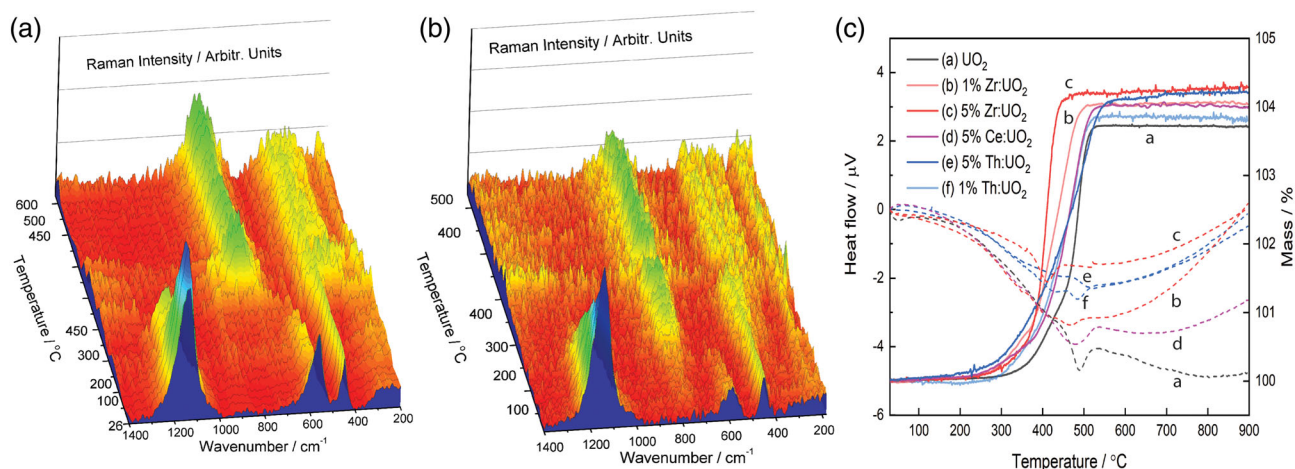


FIGURE 5 Evolution of Raman spectra of (a) undoped UO_2 and (b) Zr-doped UO_2 heated in air to 600°C . Temperature was held at 450°C to observe oxidation before heating continued. Spectra measured with 532 nm laser. (c) TGA/DSC of doped and undoped UO_2 . Heating was done in air to 900°C [Colour figure can be viewed at wileyonlinelibrary.com]

(or U_3O_7) phase in the doped UO_2 at low temperature, as previously proposed by McEachern et al.^[67] This hypothesis is also supported by the in situ high temperature Raman in this work (Figure 5b) that U_3O_8 -like signatures are evidenced in the Zr:UO_2 even below 200°C , which can be attributed to U_3O_7 or U_4O_{9+y} due to their proposed similarity in structure.^[68] Moreover, the TGA curves of 6.7 at.% Zr-doped UO_2 (also 5% Th-doped UO_2) has only one oxidation step to U_3O_8 , compared with the typical two steps ($\text{UO}_2 \rightarrow \text{U}_4\text{O}_{9+y}/\text{U}_3\text{O}_7 \rightarrow \text{U}_3\text{O}_8$) for undoped UO_2 ,^[16,69] both of which are consistent with the differences observed in the two cases of temperature dependent Raman spectra.

Recent computational studies on lanthanide-doped UO_2 ^[22] have shown that trivalent cation size influences oxidation, in that the strain associated with small cations results in stabilization from further contraction upon oxidation; this result is supported by our previous investigations where Yb:UO_2 showed delayed oxidation compared with Nd:UO_2 .^[1] In the case here, there may be a different effect, because Zr is considerably smaller than Th and results in worse oxidation, but the charge compensation mechanism is not present, so the effects of oxygen vacancies and interstitials will be different for the tetravalent dopants. The structural mechanisms of the differences in oxidation behavior of these doped materials thus need further exploration, such as with in situ Raman studies as shown here.

4 | MAPPING UO_2

4.1 | Raman maps

Raman spectral maps can be generated using a number of different parameters. For example, the intensity,

position, or integrated area of a specific peak can be used to show differences in spectral features as a function of position on the sample. A correlation spectrum can also be used to show relative similarity to a reference spectrum. Raman maps using T_{2g} peak intensity profile were collected on an undoped UO_2 sample using 532 nm (Figure 6a) and 785 nm (Figure 6b) lasers. Mapping the T_{2g} intensity with both lasers provides a clear distinction between grains. T_{2g} peaks with a higher intensity are highlighted in red on the map. Although individual spectra are comparable, the 785 nm laser produced sharper and more detailed maps. We also attempted mapping with the 455 nm laser but did not achieve good results.

The ratio of the defect band to T_{2g} band area or intensity can be used to estimate the amount of defects present in UO_2 .^[4] A map was also created using the total defect band/ T_{2g} area ratio, but this was not found to provide any additional information over using only T_{2g} intensity, possibly indicating that the intrinsic defect concentration in this sample is low and homogeneously distributed across the scanned zone. Better spatial resolution was achieved in the T_{2g} intensity map than with area ratio maps. Other profiles such as 2LO intensity or T_{2g} position did not result in useful maps but may be insightful for more heavily oxidized samples with a greater number of defects.

4.2 | Mapping with crystallographic orientation

EBSB is a powerful technique that can be used to obtain grain size distributions and crystallographic orientations. Maslova et al.^[40] measured a UO_2 sample with EBSB and calculated theoretical T_{2g} intensities. T_{2g} intensity

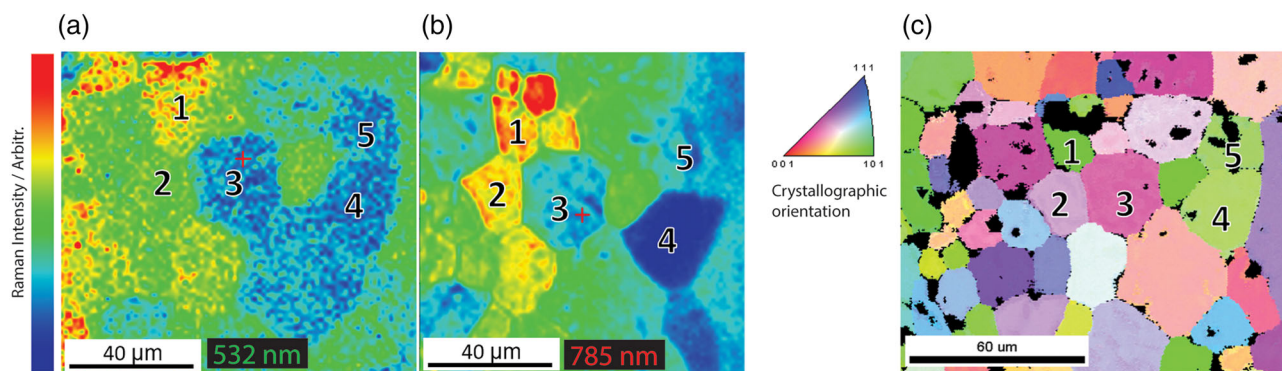


FIGURE 6 Raman maps of the same area generated from T_{2g} peak intensity, measured with the 532 nm laser (left) and 785 nm (middle), and electron backscatter diffraction (EBSD) map with [100] pole figure key, showing crystallographic orientations of each grain [Colour figure can be viewed at wileyonlinelibrary.com]

maps were also measured with a 633 nm vertically polarized laser. The authors found that the theoretical calculations were correlated well with Raman measurements in most areas and attributed poorer correlated areas to minor difference in stoichiometry or residual strains.

Analogous EBSD measurements were performed on our undoped UO_2 sample. An average grain size of 15.25 μm with standard deviation 7 μm was calculated, and texture analysis about $\langle 100 \rangle$, $\langle 110 \rangle$, and $\langle 111 \rangle$ normal directions confirm that grains are randomly oriented. Black areas in the EBSD map (Figure 6c) are removed data points that could not be properly indexed, likely due to porosity.

EBSD maps may also be used in combination with Raman mapping to investigate any changes in oxidation behavior based on grain orientations. Attempts to collect maps during in situ heating experiment were not successful using the 785 nm laser, in part due to difficulties measuring U_3O_8 using this wavelength as described previously, illustrating compromises with laser wavelength choice. To obtain good maps, a smooth sample surface is needed. However, the small pieces of UO_2 used (<200 mg) broke apart during oxidation, leaving the laser unfocused. Using a 532 nm laser could potentially allow measurements at higher temperature once U_3O_8 begins to form. Although the 2LO band did not provide useful maps in the annealed UO_2 sample, the sensitivity of the 2LO band to oxidation could prove beneficial for measuring small differences between grains in in situ oxidation experiments.^[27]

4.3 | Laser-induced luminescence

Rare-earth ions having unfilled f orbitals will luminesce with f - f electronic transitions when excited with appropriate energies (e.g., Nd^{3+} and 785 nm excitation).^[70] When this occurs, a very intense signal is measured by the spectrometer,^[71,72] provided that the grating allows for collection of the light at the emitted wavelength and the integration time is long enough. What is in many cases seen as a problem with laser-induced fluorescence in Raman spectroscopy, here is used as a tool, as in other studies.^[13,73–75] In the case of UO_2 , the electron density and band gap cause a large amount of self-absorption of any emitted light, compared with analogous rare-earth doped matrices like CeO_2 . Despite these challenges, emissions can be observed in rare-earth-doped UO_2 when the dopants are present in sufficient quantity. In our case, we investigate the distribution of Nd^{3+} in UO_2 , using a 785 nm laser to excite the $^4\text{F}_{3/2}$ to $^4\text{I}_{9/2}$ Stark-level manifold of Nd^{3+} ,

which is evident in the 850–930 nm range ($\sim 1,200$ – 2000 cm^{-1} Raman shift for 785 nm excitation) (see Figure S12).

To assess the utility of this technique, we examine UO_2 samples doped with 5 to 40 at.% Nd. In this study, we see at least five transitions, but the details of these depend on the Nd concentration, and the signature is not necessarily uniform across the samples (see Figure 7a). However, with increasing Nd, the luminescence bands in this range become sharper. For one pellet, the ~ 10 at.% Nd: UO_2 , we investigated further using imaging. On initial imaging, light and dark grey regions visible using optical microscopy suggest some phase segregation (Figure 7c). Raman spectroscopy shows that the light grey regions are similar to other lower concentration Nd-doped samples^[1] with a small T_{2g} peak and a relatively large defect band (Figure 7b). There are additional features around 390 and 1400 cm^{-1} that become more prominent in the darker regions, for which we observe more intense luminescence bands around 1200 and 1600 cm^{-1} , similar to those in Nd_2O_3 (Figure 7b). A Raman map was generated using Nd_2O_3 as a correlation spectrum representative of Nd^{3+} luminescence (Figure 7d). Note that this correlation map does not imply that all Nd^{3+} is present as crystalline Nd_2O_3 , rather that the spectrum in some areas is more similar to Nd_2O_3 than UO_2 , most notably in the luminescence region. Measurement of four different suppliers of Nd_2O_3 , two shown in Figure 7a, indicates that the details in the Stark manifold of interest can vary widely, but are the most prominent features of the spectrum when excited in this way. In the correlation map (Figure 7d), areas in red are more closely correlated to Nd_2O_3 , although the blue regions are less so. SEM-EDS analysis of a similar region (Figure 7e) show distinct areas with higher (7.36 at.%) and lower (3.38 at.%) Nd concentrations, respectively, as determined by semi-quantitative EDS.

X-ray diffraction (XRD) of these samples, see Figure S13, indicates a single phase of fluorite structure, even at the highest level of Nd_2O_3 , which is ideally $\text{U}_{0.6}\text{Nd}_{0.4}\text{O}_{2-x}$ (i.e., sample name Nd40). There is some debate in the literature as to whether there is a miscibility gap in the UO_2 - Nd_2O_3 solid solution. Some authors state that at high levels of Nd incorporation ($\text{Nd} > 6 \text{ wt}\%$), there are two face-centered cubic (FCC) phases, where one phase is oxygen stoichiometric UO_2 with Nd^{3+} charge compensated by U^{5+} ions, although the other phase is hypostoichiometric where Nd^{3+} is charge compensated by oxygen vacancy formation.^[30,76] Later, it was argued that these differences were rather a function of sample preparation and that longer holding time during initial preparation resulted in a lower disorder on the

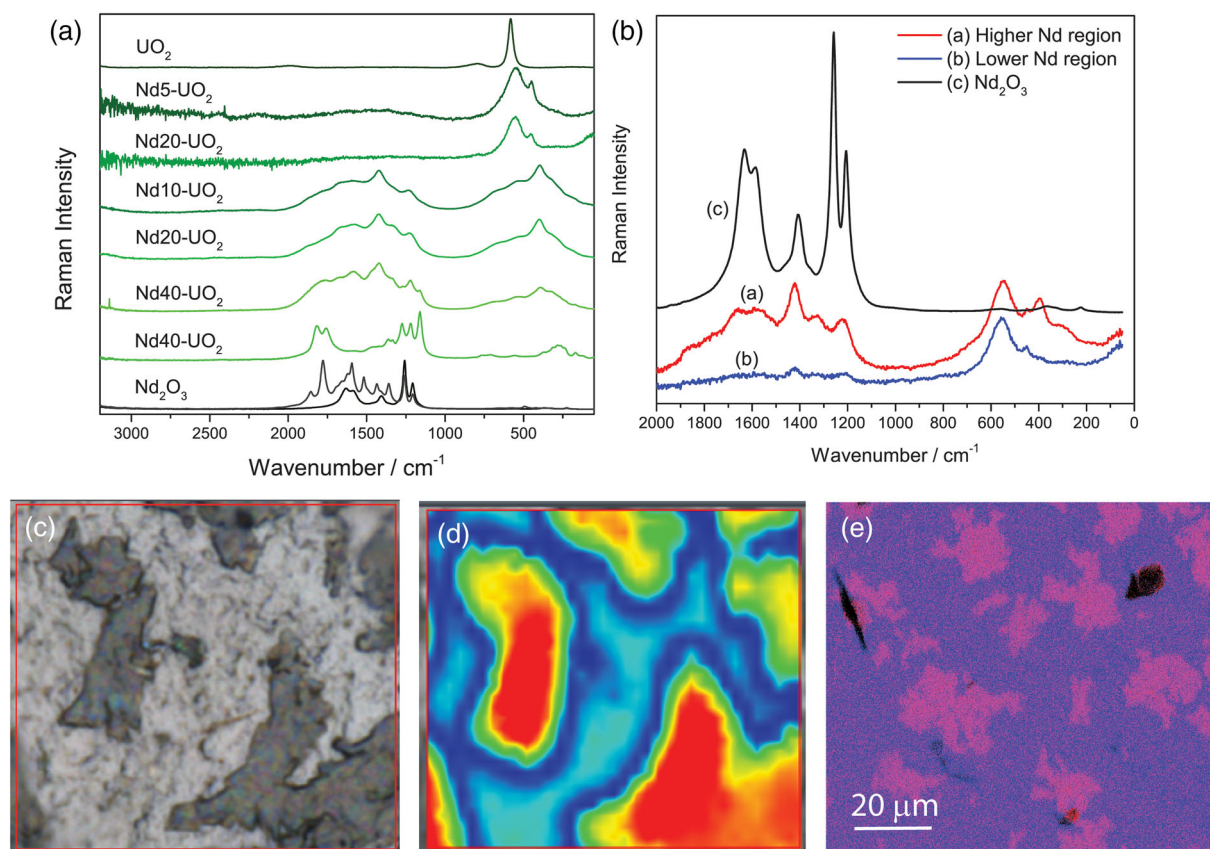


FIGURE 7 Use of luminescence features for imaging. (a) Comparison of Raman spectra collected from different regions of several Nd: UO_2 samples, compared with two different Nd_2O_3 powdered oxides. (b) Raman spectra from different regions of 10% Nd-doped UO_2 pellet and from Nd_2O_3 , collected using a 785 nm laser, compared with an Nd_2O_3 correlation spectrum. (c) Optical image from the Raman microscope and (d) Raman map of the same region colored according to correlation with Nd_2O_3 spectrum. (e) Energy dispersive spectroscopy (EDS) composite map of 10% Nd-doped UO_2 where red is Nd and blue is U [Colour figure can be viewed at wileyonlinelibrary.com]

U/Nd lattice and that oxygen vacancies were always responsible for the charge compensation.^[77] When conditions of synthesis are used to control the hypostoichiometry, a single-phase fluorite lattice can be produced at least up to $\text{U}_{0.75}\text{Nd}_{0.25}\text{O}_2$ (i.e., 25Nd), even when subsequently treated with reducing conditions.^[78] Though answering this debated question about the UO_2 - Nd_2O_3 phase diagram was not the purpose of this study, it is demonstrated that use of luminescence features while collecting Raman spectra can aid in identifying such effects.

Evidently, especially for lanthanide (i.e., representative fission product) doping in UO_2 , luminescence transitions and mapping of these can be a useful tool for determining heterogeneities even in the highly absorbing UO_2 matrix. One could imagine, for instance, applying this technique to understand microstructure of Gd-doped UO_2 accident tolerant fuels,^[16] where the

luminescence mapping was performed on trace rare-earth impurities from the Gd precursor. For other trivalent rare earths, a different excitation laser would be recommended, depending on the energies of the transition manifolds.^[13] Laser-induced luminescence mapping has also been shown to be useful for studies involving radiation damage, such as in zircons and other accessory minerals.^[74]

5 | CONCLUSIONS

A combination of different Raman excitation wavelengths (455, 532, and 785 nm) provides complementary data on the defects present in uranium oxides but also presents necessary compromises. The 532 nm laser provides great sensitivity to the 1LO and 2LO bands due to resonance with the electronic band gap. The 785 nm laser

was most effective in analyzing the 540 cm^{-1} V_O band, providing greater sensitivity for doping as opposed to irradiation, and providing improved Raman mapping features. In heat stage experiments, the 532 nm laser provided good spectra for both UO_2 and U_3O_8 , allowing continuous measurements during heating without readjusting laser focus or power. Spectra from U_3O_8 were of poor quality when measured with the 785 nm laser, whereas the 455 nm laser resulted in the lowest quality spectra from UO_2 . Much lower power was needed with the 455 nm laser to prevent damaging the sample, but the spectra produced did allow more focus on irradiation changes even in the presence of doping. Long exposure times also were seen to damage the sample making it difficult to acquire low noise, pristine spectra. For direct excitation of rare-earth transitions, the correct excitation laser combined with the grating is required. For Nd^{3+} , frequently used in studies with UO_2 , the 785 nm laser is ideal as it allows acquisition of an important manifold of electronic $f-f$ transitions.

Using a combination of Raman excitation wavelengths can provide complementary information on the defects and oxidation state. For the current studies, the recommended conditions are as follows.

- 455 nm: U_3O_8 , 2LO, irradiation defects
- 532 nm: U_3O_8 , UO_2 , 1LO/2LO, irradiation defects, mapping, heat stage
- 785 nm: UO_2 , oxidation and doping defects, mapping, heat stage (only if minimal oxidation), Nd^{3+} luminescence excitation.

The summary provided here of the utility of multi-wavelength Raman investigation of UO_2 can be applied to future studies of nuclear fuel microstructures and spent fuel as follows. First, choice of the particular laser wavelength allows focus on particular defects of interest due to the presence of a resonant LO band in the typically measured “defect band”. Second, the use of fission products as local luminescent spectroscopic probes may allow creation of spatial maps showing degree of fuel burnup, even on real irradiated fuel. In situ collected Raman spectra obtained under different gas environments, especially when compared with other measurements of oxidation such as TGA, promise to provide insight into the effect of dopants on oxidation pathways in UO_2 , perhaps contributing to the design of more stable fuels under irradiation and subsequent storage conditions. Finally, spatial mapping of polycrystalline ceramic UO_2 and comparison with crystallographic data may aid understanding of crystallite orientation-dependent oxidation behavior, and any relation to oxygen stoichiometry as modulated by dopants.

ACKNOWLEDGEMENTS

The authors wish to acknowledge funding for this project from U.S. Department of Energy Nuclear Energy University Program award # DE-NE0008689 and funding for the purchase of the Raman microscope from the U.S. Department of Energy Office of River Protection award # 89304017CEM000001. The authors would like to thank the Dalton Cumbrian Facility (DCF) science research center at the University of Manchester for their support and engagement in the irradiation experiment. The UK collaborators thank the UK Engineering and Physical Sciences Research Council (EPSRC) for funding under grant agreements EP/N017374/1 and EP/R006075/1.

CONFLICT OF INTEREST

On behalf of all authors, the corresponding author states that there is no conflict of interest.

DATA AVAILABILITY STATEMENT

The datasets generated and analyzed during the current study are available from the corresponding author upon reasonable request.

ORCID

John McCloy  <https://orcid.org/0000-0001-7476-7771>

REFERENCES

- [1] T. A. Olds, S. E. Karcher, K. W. Kriegsman, X. Guo, J. S. McCloy, *J. Nucl. Mater.* **2020**, 530, 151959.
- [2] Z. Talip, T. Wiss, P. E. Raison, J. Paillier, D. Manara, J. Somers, R. J. M. Konings, *J. Am. Ceram. Soc.* **2015**, 98, 2278.
- [3] J. M. Elorrieta, L. J. Bonales, M. Naji, D. Manara, V. G. Baonza, J. Cobos, *J. Raman Spectros.* **2018**, 49, 878.
- [4] M. Razdan, D. W. Shoesmith, *J. Electrochem. Soc.* **2013**, 161, H105.
- [5] R. Mohun, L. Desgranges, A. Canizarès, N. Raimboux, F. Duval, R. Omnee, C. Jégou, S. Miro, P. Simon, *J. Nucl. Mater.* **2018**, 509, 305.
- [6] T. L. Spano, A. Simonetti, L. Corcoran, P. A. Smith, S. R. Lewis, P. C. Burns, *J. Nucl. Mater.* **2019**, 518, 149.
- [7] T. Livneh, *J. Phys. Cond. Matt.* **2008**, 20, 085202.
- [8] T. Livneh, *Phys. Rev. B* **2022**, 105, 045115.
- [9] T. Livneh, E. Sterer, *Phys. Rev. B* **2006**, 73, 1.
- [10] H. He, Z. Ding, D. W. Shoesmith, *Electrochem. Comm.* **2009**, 11, 1724.
- [11] O. A. Maslova, G. Guimbretière, M. R. Ammar, L. Desgranges, C. Jégou, A. Canizarès, P. Simon, *Mater. Char.* **2017**, 129, 260.
- [12] J. Bruno, R. C. Ewing, *Elements* **2006**, 2, 343.
- [13] C. Lenz, L. Nasdala, D. Talla, C. Hauzenberger, R. Seitz, U. Kolitsch, *Chem. Geol.* **2015**, 415, 1.
- [14] H. He, R. K. Zhu, Z. Qin, P. Keech, Z. Ding, D. W. Shoesmith, *J. Electrochem. Soc.* **2009**, 156, C87.
- [15] B. Grambow, *Spent fuel dissolution and oxidation. An evaluation of literature data*, SKB, Stockholm, TR **1989** 89.

- [16] R. D. Scheele, B. D. Hanson, A. M. Casella, *J. Nucl. Mater.* **2021**, 552, 153008.
- [17] F. Tocino, S. Szenknect, A. Mesbah, N. Clavier, N. Dacheux, *Prog. Nucl. Energy* **2014**, 72, 101.
- [18] L. Desgranges, Y. Ma, P. Garcia, G. Baldinozzi, D. Siméone, H. E. Fischer, *Inorg. Chem.* **2017**, 56, 321.
- [19] M. L. Palacios, S. H. Taylor, *Appl. Spectros.* **2000**, 54, 1372.
- [20] A. Miskowicz, T. Spano, R. Hunt, A. E. Shields, J. L. Niedziela, S. Finkeldei, *Phys. Rev. Mater.* **2020**, 4, 093610.
- [21] L. Desgranges, G. Baldinozzi, G. Rousseau, J.-C. Nièpce, G. Calvarin, *Inorg. Chem.* **2009**, 48, 7585.
- [22] V. L. Vinograd, A. A. Bukaemskiy, G. Modolo, G. Deissmann, D. Bosbach, *Front. Chem.* **2021**, 9, 705024.
- [23] D. W. Shoemsmith, *J. Nucl. Mater.* **2000**, 282, 1.
- [24] A. Casella, "The dissolution rate of unirradiated UO₂ under repository conditions: the influence of fuel and water chemistry, dissolved oxygen, and temperature," Nuclear Engineering, University of Missouri, **2008**.
- [25] A. Casella, B. Hanson, W. Miller, *J. Nucl. Mater.* **2016**, 476, 45.
- [26] R. Rao, R. K. Bhagat, N. P. Salke, A. Kumar, *Appl. Spectros.* **2014**, 68, 44.
- [27] K. Rickert, T. A. Prusnick, M. M. Kimani, E. A. Moore, C. A. Merriman, J. M. Mann, *J. Nucl. Mater.* **2019**, 514, 1.
- [28] D. Manara, B. Renker, *J. Nucl. Mater.* **2003**, 321, 233.
- [29] H. He, D. Shoemsmith, *Phys. Chem. Chem. Phys.* **2010**, 12, 8108.
- [30] L. Desgranges, G. Baldinozzi, P. Simon, G. Guimbretière, A. Canizares, *J. Raman Spectros.* **2012**, 43, 455.
- [31] L. Desgranges, G. Guimbretière, P. Simon, F. Duval, A. Canizares, R. Omnee, C. Jégou, R. Carballo, *Nucl. Instr. Meth. B* **2014**, 327, 74.
- [32] R. Mohun, L. Desgranges, P. Simon, A. Canizarès, N. Raimboux, R. Omnee, C. Jégou, S. Miro, *Proced. Chem.* **2016**, 21, 326.
- [33] R. Mohun, "Raman spectroscopy for the characterization of defective spent nuclear fuels during interim storage in pools," Physique théorique et Mathématique, Université d'Aix-Marseille, **2017**.
- [34] S. Singh, S. K. Gupta, Y. Sonvane, K. A. Nekrasov, A. Y. Kupryazhkin, P. N. Gajjar, *J. Nucl. Mater.* **2018**, 511, 128.
- [35] N. H. H. Phuc, T. Okuno, A. Matsuda, H. Muto, *J. Europ. Ceram. Soc.* **2014**, 34, 1009.
- [36] S. Stewart, R. J. Priore, M. P. Nelson, P. J. Treado, *Annu. Rev. Anal. Chem.* **2012**, 5, 337.
- [37] F. Prado Araujo, N. Hulsbosch, P. Muchez, *J. Raman Spectros.* **2021**, 52, 690.
- [38] J.-y. Colle, D. Manara, R. J. M. Konings, *Spectros. Eur.* **2020**, 32, 9.
- [39] O. A. Maslova, X. Iltis, L. Desgranges, M. R. Ammar, C. Genevois, E. de Bilbao, A. Canizarès, S. A. Barannikova, I. N. Leontyev, P. Simon, *Mater. Char.* **2019**, 147, 280.
- [40] O. A. Maslova, X. Iltis, L. Desgranges, G. Guimbretière, M. R. Ammar, C. Genevois, E. de Bilbao, A. Canizares, S. A. Barannikova, I. N. Leontyev, P. Simon, *AIP Conf. Proc.* **2018**, 2051, 020189.
- [41] L. Desgranges, G. Baldinozzi, D. Siméone, H. E. Fischer, *Inorg. Chem.* **2011**, 50, 6146.
- [42] K. Rickert, T. A. Prusnick, E. Hunt, M. M. Kimani, S. Chastang, D. L. Brooks, E. A. Moore, J. C. Petrosky, J. M. Mann, *J. Nucl. Mater.* **2019**, 517, 254.
- [43] F. Menges, "Spectragraph-optical spectroscopy software." **2020**.
- [44] M. Wojdyr, *J. Appl. Crystallog.* **2010**, 43, 1126.
- [45] A. C. Strzelecki, K. Kriegsman, P. Estevenon, V. Goncharov, J. Bai, S. Szenknect, A. Mesbah, D. Wu, J. S. McCloy, N. Dacheux, X. Guo, *ACS Earth Space Chem.* **2020**, 4, 2129.
- [46] E. A. Stefaniak, A. Alsecz, I. E. Sajó, A. Worobiec, Z. Máthé, S. Török, R. V. Grieken, *J. Nucl. Mater.* **2008**, 381, 278.
- [47] H. Shi, M. Chu, P. Zhang, *J. Nucl. Mater.* **2010**, 400, 151.
- [48] J. Schoenes, *Phys. Rep.* **1980**, 63, 301.
- [49] C. Nguyen Trung, G. M. Begun, D. A. Palmer, *Inorg. Chem.* **1992**, 31, 5280.
- [50] T. Fujii, K. Fujiwara, H. Yamana, H. Moriyama, *J. Alloys Compds.* **2001**, 323-324, 859.
- [51] Z. Gajek, M. P. Lahalle, J. C. Krupa, J. Mulak, *J. Less-Common Met.* **1988**, 139, 351.
- [52] J. Lee, C. Kwon, J. Kim, Y. S. Youn, J. Y. Kim, B. Han, S. H. Lim, *Int. J. Energy Res.* **2019**, 43, 3322.
- [53] L. Li, F. Chen, J. Q. Lu, M. F. Luo, *J. Phys. Chem. A* **2011**, 115, 7972.
- [54] R. D. Shannon, *Acta Cryst. A* **1976**, 32, 751.
- [55] J.-G. Kim, Y.-K. Ha, S.-D. Park, K.-Y. Jee, W.-H. Kim, *J. Nucl. Mater.* **2001**, 297, 327.
- [56] J. F. Ziegler, J. P. Biersack, U. Littmark, *The Stopping and Range of Ions in Solids*, Springer, Pergamon, New York **1985**.
- [57] G. Guimbretière, L. Desgranges, A. Canizarès, G. Carlot, R. Carballo, C. Jégou, F. Duval, N. Raimboux, M. R. Ammar, P. Simon, *Appl. Phys. Lett.* **2012**, 100, 251914.
- [58] G. Guimbretière, A. Canizarès, N. Raimboux, J. Joseph, P. Desgardin, L. Desgranges, C. Jégou, P. Simon, *J. Raman Spectros.* **2015**, 46, 418.
- [59] R. I. Palomares, J. Shamblin, C. L. Tracy, J. Neufeind, R. C. Ewing, C. Trautmann, M. Lang, *J. Mater. Chem. A* **2017**, 5, 12193.
- [60] W. F. Cureton, C. L. Tracy, M. Lang, *Quant. Beam Sci.* **2021**, 5, 19.
- [61] J. M. Elorrieta, L. J. Bonales, N. Rodríguez-Villagra, V. G. Baonza, J. Cobos, *Phys. Chem. Chem. Phys.* **2016**, 18, 28209.
- [62] G. Rousseau, L. Desgranges, F. Charlot, N. Millot, J. C. Nièpce, M. Pijolat, F. Valdivieso, G. Baldinozzi, J. F. Bélar, *J. Nucl. Mater.* **2006**, 355, 10.
- [63] I. S. Butler, G. C. Allen, N. A. Tuan, *Appl. Spectros.* **1988**, 42, 901.
- [64] S. D. Senanayake, R. Rousseau, D. Colegrave, H. Idriss, *J. Nucl. Mater.* **2005**, 342, 179.
- [65] A. Miskowicz, J. L. Niedziela, T. L. Spano, M. W. Ambrogio, S. Finkeldei, R. Hunt, A. E. Shields, *J. Nucl. Mater.* **2019**, 527, 151790.
- [66] W. J. Siekhaus, *MRS Proc.* **2003**, 802(DD5), 10.
- [67] R. J. McEachern, D. C. Doern, D. D. Wood, *J. Nucl. Mater.* **1998**, 252, 145.
- [68] D. A. Andersson, G. Baldinozzi, L. Desgranges, D. R. Conradson, S. D. Conradson, *Inorg. Chem.* **2013**, 52, 2769.
- [69] R. J. McEachern, P. Taylor, *J. Nucl. Mater.* **1998**, 254, 87.
- [70] C. Lenz, D. Talla, K. Ruschel, R. Skoda, J. Gotze, L. Nasdala, *Mineral. Petrol.* **2013**, 107, 415.
- [71] E. S. Fotso Gueutue, A. Canizares, P. Simon, N. Raimboux, L. Hennes, M. R. Ammar, *J. Raman Spectros.* **2018**, 49, 822.
- [72] O. Beysac, *Elements* **2020**, 16, 117.

- [73] O. Beyssac, J. D. Pasteris, *Elements* **2020**, *16*, 87.
- [74] C. Lenz, G. Thorogood, R. Aughterson, M. Ionescu, D. J. Gregg, J. Davis, G. R. Lumpkin, *Front. Chem.* **2019**, *7*, 13.
- [75] J. Yu, L. Cui, H. He, Y. Hu, H. Wu, J. Zeng, Y. Liu, *Chem. Phys. Lett.* **2012**, *549*, 32.
- [76] G. Dottavio, Y. Pontillon, L. Desgranges, R. C. Belin, J. C. Richaud, J. Noirot, *C. Valot.* **2014**, *72*, 22.
- [77] R. I. Barabash, S. L. Voit, D. S. Aidhy, S. M. Lee, T. W. Knight, D. J. Sprouster, *L. E. Ecker.* **2015**, *30*, 3026.
- [78] B. Herrero, R. Bès, F. Audubert, N. Clavier, M. O. J. Y. Hunault, G. Baldinozzi, *J. Nucl. Mater.* **2020**, *539*, 152276.

SUPPORTING INFORMATION

Additional supporting information may be found in the online version of the article at the publisher's website.

How to cite this article: S. Karcher, R. Mohun, T. Olds, M. Weber, K. Kriegsman, X. Zhao, X. Guo, C. Corkhill, D. Field, J. McCloy, *J Raman Spectrosc* **2022**, *1*. <https://doi.org/10.1002/jrs.6321>